



Citation for published version:

Wu, Z, Zhu, ZQ, Wang, C, Mipo, JC, Personnaz, S & Farah, P 2020, 'Analysis and Reduction of On-Load DC Winding Induced Voltage in Wound Field Switched Flux Machines', *IEEE Transactions on Industrial Electronics*, vol. 67, no. 4, 8701561, pp. 2655-2666. <https://doi.org/10.1109/TIE.2019.2912779>

DOI:

[10.1109/TIE.2019.2912779](https://doi.org/10.1109/TIE.2019.2912779)

Publication date:

2020

Document Version

Peer reviewed version

[Link to publication](#)

University of Bath

Alternative formats

If you require this document in an alternative format, please contact:
openaccess@bath.ac.uk

General rights

Copyright and moral rights for the publications made accessible in the public portal are retained by the authors and/or other copyright owners and it is a condition of accessing publications that users recognise and abide by the legal requirements associated with these rights.

Take down policy

If you believe that this document breaches copyright please contact us providing details, and we will remove access to the work immediately and investigate your claim.

Analysis and Reduction of On-Load DC Winding Induced Voltage in Wound Field Switched Flux Machines

Z. Z. Wu, *Member, IEEE*, Z. Q. Zhu, *Fellow, IEEE*, C. Wang, J. C. Mipo, S. Personnaz, and P. Farah

Abstract—DC winding induced voltage pulsation in wound field switched flux (WFSF) machines causes DC winding current ripple and field excitation fluctuation, challenges the DC power source and deteriorates the control performance. Hence, reducing this pulsation is important in the design of a WFSF machine. In this paper, based on the analytical models, rotor skewing and rotor iron piece pairing are proposed and comparatively investigated by the finite element (FE) method to reduce the on-load DC winding induced voltage in WFSF machines having partitioned stators and concentrated AC windings. FE results show that peak to peak value of the on-load DC winding induced voltage in the analysed 12/10-pole partitioned stator WFSF (PS-WFSF) machines can be reduced by 78.42% or 77.16% by using rotor skewing or rotor pairing, respectively, whilst the torque density can be maintained by >90%. As for the 12/11-, 12/13- and 12/14-pole PS-WFSF machines, by using rotor iron piece inner arc pairing, the on-load DC winding induced voltage can be reduced by 64.11%, 52.12% and 76.49%, respectively, whilst the torque density can also be maintained by more than 90%. Prototypes are built and tested to verify the analytical and FE results.

Index Terms—AC winding, DC winding, DC winding induced voltage, field winding, on-load DC winding induced voltage, rotor iron piece pairing, skewing, vernier reluctance machine.

I. INTRODUCTION

WOUND field synchronous machines (WFSMs) are cheaper than rare-earth permanent magnet (PM) synchronous machines due to the high price of rare-earth PM material, and hence become a hot research topic recently [1].

Manuscript received May 24, 2018; revised November 23, 2018 and March 6, 2019; accepted March 28, 2019. (*Corresponding author: Z. Q. Zhu.*)

Z. Z. Wu is with Department of Mechanical Engineering, University of Bath, Bath, U.K. (z.z.wu@bath.ac.uk).

Z. Q. Zhu, and C. Wang are with the Electrical Machines and Drives Group, University of Sheffield, Sheffield, U.K. (z.q.zhu@sheffield.ac.uk, cwang55@sheffield.ac.uk).

J. C. Mipo, S. Personnaz, and P. Farah are with Valeo Powertrain Electric Systems, 94017 Créteil Cedex, France (jean-claude.mipo@valeo.com, sophie.personnaz@valeo.com, philippe.farah@valeo.com).

WFSMs can be divided into two categories according to the position of the DC field winding, i.e. the wound-rotor synchronous machines (WRSMs) having DC winding in the rotor and the vernier reluctance machines (VRMs) with both DC and AC windings placed in the stator, which has been proposed for more than 50 years [2], [3]. Compared with the conventional WRSMs, the VRMs [2]-[8] perform without slips and brushes, and hence higher stability and reliability. Compared with switched reluctance machines (SRMs) [9], VRMs can exhibit smaller torque ripple and noise due to the nearly sinusoidal AC winding back-electromotive forces (back-EMFs) [10], but the simplicity and robustness of the SRMs can be retained in the VRMs.

Several machine topologies are proposed and analyzed by finite element (FE) method for VRMs [11]-[16], including both single phase [11], [12] and 3-phase counterparts [13]-[16]. Besides the well-established FE analysis, analytical solutions have been widely used to fast predict the air-gap field distribution and design the VRMs, including both subdomain method [17]-[19] and magnemotive force-permeance method [6]. Efforts are also made to realize the industrial applications of VRMs, as studied in [12] for the low-cost single phase counterpart with a simple and compact controller, and in [8], [20]-[22] for potentially applying the 3-phase counterparts in traction applications. In [23], for further enhancing the torque density, a new type of VRM, the so-called partitioned stator (PS) wound field switched flux (WFSF) (PS-WFSF) machine in which the AC armature and DC field windings are separately accommodated in two stators is proposed, as shown in Fig. 1 for the 12/10-pole counterpart. Compared with the conventional single stator WFSF machine [13], the PS-WFSF machine can offer a higher torque density due to a higher total slot area and a better utilization of space. As shown in TABLE I of which details can be referred in Appendix A, compared with ferrite surface-mounted PM (SPM) machine, the PS-WFSF machine exhibits 46.91% higher torque per unit volume, however, the efficiency is only 13.39% larger due to DC winding copper loss. Although the rated torque of the PS-WFSF machine is smaller than that of the conventional WRSM, their efficiencies are similar, i.e. 87.78% and 90.60%, respectively, since the conventional WRSM having overlapping AC windings suffers from a longer end winding and hence a higher copper loss. In [8], it is recommended that

the torque density of the VRMs can be improved by using high-temperature winding insulation, whilst the efficiency can be enhanced by applying thinner laminations to minimize the iron losses. Moreover, since both DC and AC windings of the PS-WFSF machines are located in the stator, the generated heat due to copper loss can be easily mitigated [10], oppositely, advanced rotor cooling is required for mitigate the rotor heat in the WRSMs. It is also worth noting that compared with WRSMs, a much more reliable rotor structure without winding or PM can be achieved in the VRMs.

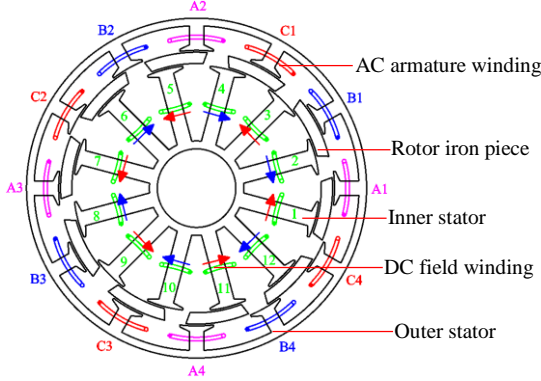


Fig. 1. Cross-section of a 12/10-stator/rotor-pole PS-WFSF machine.

In [25], it is found that due to the variation of air-gap permeance, the PS-WFSF machines suffer from open-circuit DC winding induced voltage, which will cause DC winding current ripple [26], [27], challenge the DC power source and deteriorate the control performance. The raised DC winding current ripple will cause a fluctuated field excitation and hence additional harmonic components in the AC winding induced voltages, with average torque and torque ripple being impacted [26]. Rotor skewing is applied to reduce the open-circuit DC winding induced voltage in [25]. Both the analytical and finite element (FE) methods show that the open-circuit DC winding induced voltage can be effectively reduced by skewing, although the AC armature winding phase fundamental back-EMF and hence the torque density will be slightly smaller.

TABLE I

COMPARISON OF PS-WFSF MACHINE, WRSM AND SPM MACHINE HAVING SAME SPACE ENVELOP AS TOYOTA PRIUS 2010 IPM MACHINE [24]

Item	Unit	PS-WFSF	WRSM	SPM
Winding current density, J_s [24]	A/mm ²	26.8	26.8	26.8
Rated rotor speed, Ω_r [24]	r/min	2795	2795	2795
Rated torque, T_r	Nm	391.19	736.81	224.16
Rated power, P_r	kW	114.50	215.66	65.61
AC windings stack copper loss, p_{cuas}	kW	3.17	3.78	5.71
AC windings end copper loss, p_{cuae}	kW	5.01	8.81	12.90
DC winding stack copper loss, p_{cufs}	kW	2.48	3.42	N/A
DC winding end copper loss, p_{cufe}	kW	3.31	5.35	N/A
Total copper loss, p_{cu}	kW	13.97	21.37	18.61
Iron loss, p_{iron}	kW	1.73	0.92	0.41
Efficiency, η	%	87.78	90.60	77.41
Axial length, l_s	mm	50	50	50
Single side AC windings height, h_{ea}	mm	28.69	41.66	40.39
Single side DC windings height, h_{ef}	mm	24.15	27.84	N/A
Axial length with end winding, l_a	mm	107.38	133.32	90.39
Machine volume, V	L	5.88	7.30	4.95
Rated torque per unit volume, TPV	Nm/L	66.55	100.96	45.30
Rated power per unit volume, PPV	kW/L	19.48	29.55	13.26

Besides skewing, pairing is another common method to

reduce harmonics in electric machines, of which the mechanism is to cancel harmonics by a pair of machine components, such as PM width pairing [28], teeth width pairing [29], pole width pairing [30]. In the rotor-PM machines in which PMs are accommodated in the rotor, PM width pairing and teeth width pairing are applied in [25] and [29] to reduce the harmonics and hence the torque ripple, respectively. In stator-PM machines with stator accommodation of PMs, rotor pole width pairing is applied in [30] to reduce the cogging torque, as there is neither winding nor PM in the rotor.

In this paper, the analysis of the open-circuit DC winding induced voltage in [25] will be extended to on-load condition, by taking the impact of armature reaction into consideration. Skewing and pairing will be comparatively investigated to reduce the on-load DC winding induced voltage. This paper is organized as follows. In section II, on-load DC winding induced voltage in the PS-WFSF machines is analytically modeled and the harmonic orders are analytically given and verified by FE results. In section III, applying rotor skewing in PS-WFSF machines to reduce the on-load DC winding induced voltage is investigated, whilst rotor pairing is applied to reduce it in section IV, followed by comparison of reduction effectiveness of various methods in section V. In section VI, prototypes are built and tested to validate the analytical and FE results, followed by conclusions in section VII.

II. ON-LOAD DC WINDING INDUCED VOLTAGE

In [25], it is found that the open-circuit DC winding induced voltage in PS-WFSF machines is caused by the variation of the air-gap permeance, exhibiting as DC winding self-inductance harmonics,

$$\psi_{ff}(\theta_e) = L_{ff}(\theta_e) \times I_f(\theta_e) \quad (1)$$

where ψ_{ff} is the open-circuit DC winding flux-linkage which is due to DC field winding current. L_{ff} is the DC winding self-inductance. θ_e is the rotor electric position.

When the saturation in the lamination steel is neglected, the on-load DC winding flux-linkage ψ_f can be divided into two parts due to DC field winding current and AC armature winding current, respectively,

$$\psi_f(\theta_e) = \psi_{ff}(\theta_e) + \psi_{fa}(\theta_e) \quad (2)$$

where ψ_{fa} is the on-load DC winding flux-linkage caused by AC armature windings, which can be divided into three parts caused by A-, B-, and C-phase currents, respectively, as,

$$\psi_{fa}(\theta_e) = \psi_{fA}(\theta_e) + \psi_{fB}(\theta_e) + \psi_{fC}(\theta_e) \quad (3)$$

where ψ_{fA} , ψ_{fB} , and ψ_{fC} are the on-load DC winding flux-linkage due to A-, B-, and C-phase currents, respectively. They can be given by,

$$\begin{cases} \psi_{fA}(\theta_e) = M_{fA}(\theta_e) \times I_A(\theta_e) \\ \psi_{fB}(\theta_e) = M_{fB}(\theta_e) \times I_B(\theta_e) \\ \psi_{fC}(\theta_e) = M_{fC}(\theta_e) \times I_C(\theta_e) \end{cases} \quad (4)$$

where M_{fA} , M_{fB} , and M_{fC} are the mutual inductances between the A-, B- and C-phase windings and the DC winding, respectively. It is worth noting that there is no DC component for M_{fA} , M_{fB} , and M_{fC} , as the open-circuit AC winding flux-linkages due to the DC winding current and these mutual inductances have no DC component in the PS-WFSF machines [23]. I_A , I_B , and I_C are

the A-, B-, C-phase currents, respectively.

In (4), M_{fA} , M_{fB} , and M_{fC} can be given by,

$$\begin{cases} M_{fA}(\theta_e) = M_{Af}(\theta_e) = \sum_{i=1,2,3,\dots}^{\infty} k_{wi} M_i \cos(i\theta_e + \theta_i) \\ M_{fB}(\theta_e) = M_{Bf}(\theta_e) = \sum_{i=1,2,3,\dots}^{\infty} k_{wi} M_i \cos\left[i\left(\theta_e - \frac{2}{3}\pi\right) + \theta_i\right] \\ M_{fC}(\theta_e) = M_{Cf}(\theta_e) = \sum_{i=1,2,3,\dots}^{\infty} k_{wi} M_i \cos\left[i\left(\theta_e + \frac{2}{3}\pi\right) + \theta_i\right] \end{cases} \quad (5)$$

where M_{Af} , M_{Bf} , and M_{Cf} are the mutual inductances between the DC winding and the A-, B- and C-phase windings, respectively. θ_i is the initial phase of the i^{th} mutual inductance harmonic. $k_{wi} M_i$ is the amplitude of the i^{th} mutual inductance harmonic, in which k_{wi} is the i^{th} harmonic winding factor,

$$k_{wi} = k_{pi} \times k_{di} \quad (6)$$

where k_{pi} and k_{di} are the i^{th} harmonic pitch and distribution factors, respectively. They can be calculated based on the analysis in [23].

In (4), when 3-phase sinusoidal currents are injected in AC winding, 3-phase currents I_A , I_B , and I_C can be given by,

$$\begin{cases} I_A = I_a \cos(\theta_e + \theta_A) \\ I_B = I_a \cos(\theta_e + \theta_A - \frac{2}{3}\pi) \\ I_C = I_a \cos(\theta_e + \theta_A + \frac{2}{3}\pi) \end{cases} \quad (7)$$

where I_a is the AC armature winding current amplitude. θ_A is the A-phase current phase angle.

Submitting (4)-(7) to (3), (3) can be simplified as,

$$\psi_{fa}(\theta_e) = \sum_{j=1,2,3,\dots}^3 \frac{3}{2} k_{pi} k_{di} M_i I_a \times \begin{cases} \cos(\theta_i - \theta_A), \text{ for } i = 1 \\ \cos[(i-1)\theta_e + \theta_i - \theta_A], \text{ for } i = 3j + 1 \\ \cos[(i+1)\theta_e + \theta_i + \theta_A], \text{ for } i = 3j - 1 \\ 0, \text{ for } i = 3j \end{cases} \quad (8)$$

where $j=1,2,3,\dots$

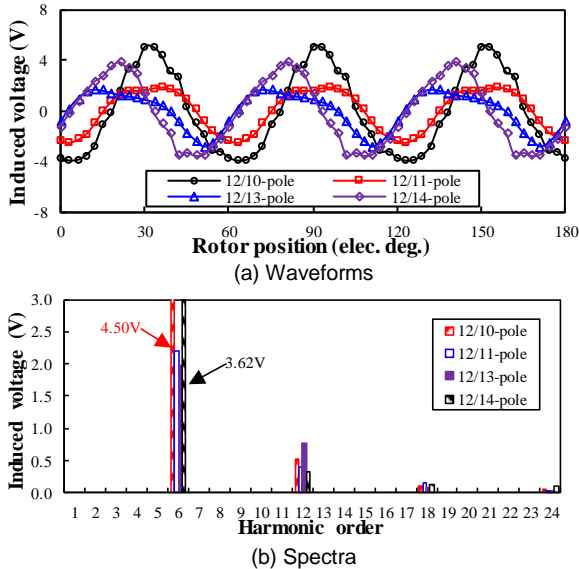


Fig. 2. On-load DC winding induced voltages at 400r/min.

As shown in (8), the cycles per electric period of the on-load DC winding flux-linkage and hence the induced-voltage N_{pe}

caused by AC winding currents ψ_{fa} is $3j$ ($j=1,2,3,\dots$). In the analyzed 12-stator-pole PS-WFSF machines having 10-, 11-, 13- and 14-rotor-pole rotors, $k_{wi}=k_{pi}k_{di}=0$ for even harmonics, as analyzed in [23]. Therefore, for the DC winding induced voltage due to armature reaction, $N_{pe}=6$ in all these 4 machines, as summarized in TABLE II. This can be evidenced by Fig. 2. As shown in TABLE II, the resulted $N_{pe}=6$ for the on-load DC winding flux-linkage for all the analyzed machines, although the N_{pe} for open-circuit condition for these machines varies, as analyzed in [25].

TABLE II
ANALYTICAL PREDICTION OF PERIODS PER ELECTRIC CYCLE N_{pe}

Item	12-stator-pole PS-WFSF machines			
	10	11	13	14
Open-circuit	6	12	12	6
Armature reaction	6	6	6	6
On-load	6	6	6	6

As shown in Fig. 2 and TABLE III, the 12/14- and 12/10-pole PS-WFSF machines suffer from higher on-load peak to peak value of DC winding induced voltage E_{pp} than the 12/13- and 12/11-pole counterparts. This is similar to that of the open-circuit DC winding induced voltage, as analyzed in [25]. In TABLE III, T_{avg} is the average rated on-load torque.

TABLE III
CHARACTERISTICS IN PS-WFSF MACHINES

Item	Unit	12-stator-pole PS-WFSF machines			
		10	11	13	14
N_r	-	10	11	13	14
Open-circuit E_{pp}	V	2.10	0.63	0.36	4.86
On-load E_{pp}	V	9.06	4.32	4.58	7.46
T_{avg}	Nm	2.97	3.07	3.21	3.34

As shown in (8), all the armature reaction DC winding flux-linkage harmonic amplitudes are proportional to both the AC armature current amplitude I_a shown in (7) and the harmonic amplitudes of the mutual inductances M_{fA} , M_{fB} , and M_{fC} shown in (5), i.e. $k_{pi}k_{di}M_i$. Since the mutual inductance harmonics shown in (5) are caused by the rotation of the salient rotor iron pieces, it can be concluded that it is the interaction between the AC armature currents shown in (7) and the mutual inductances M_{fA} , M_{fB} , and M_{fC} shown in (5) that produce the armature reaction DC winding flux-linkage harmonics and hence the induced voltage pulsation, and hence contribute to those for the on-load operation condition.

III. REDUCTION OF ON-LOAD DC WINDING INDUCED VOLTAGE BY ROTOR SKEWING

In [25] rotor skewing is proposed to reduce the open-circuit DC winding induced voltage. The results show that the open-circuit DC winding induced voltage can be effectively reduced, although the AC winding phase fundamental back-EMF will be slightly smaller. In this section, skewing is applied to reduce the on-load DC winding induced voltage, as shown as follows.

A. Conventional Optimal Skewing Angle

The on-load DC winding flux-linkage ψ_f can be divided into two parts from DC field winding current and AC armature winding current, respectively. Similar to the analysis of DC winding self-inductance L_{ff} in [25], when the rotor is continuously skewed with a skewing angle θ_{sk} , M_{fA} , M_{fB} , and

M_{fC} in (5) and ψ_{fa} in (8) can be modified as,

$$\begin{cases} M_{fA}(\theta_e) = \sum_{i=1,2,3,\dots}^{\infty} \frac{2k_{wi}M_i}{i\theta_{sk}} \cos(i\theta_e + \theta_i) \sin\left(\frac{i\theta_{sk}}{2}\right) \\ M_{fB}(\theta_e) = \sum_{i=1,2,3,\dots}^{\infty} \frac{2k_{wi}M_i}{i\theta_{sk}} \cos\left[i\left(\theta_e - \frac{2}{3}\pi\right) + \theta_i\right] \sin\left(\frac{i\theta_{sk}}{2}\right) \\ M_{fC}(\theta_e) = \sum_{i=1,2,3,\dots}^{\infty} \frac{2k_{wi}M_i}{i\theta_{sk}} \cos\left[i\left(\theta_e + \frac{2}{3}\pi\right) + \theta_i\right] \sin\left(\frac{i\theta_{sk}}{2}\right) \end{cases} \quad (9)$$

and

$$\psi_{fa}(\theta_e) = \sum \frac{3k_{pi}k_{di}M_iI_a}{i\theta_{sk}} \begin{cases} \cos(\theta_i - \theta_A) \sin\left(\frac{i\theta_{sk}}{2}\right), \text{ for } i = 1 \\ \cos[(i-1)\theta_e + \theta_i - \theta_A] \sin\left(\frac{i\theta_{sk}}{2}\right), \text{ for } i = 3j+1 \\ \cos[(i+1)\theta_e + \theta_i + \theta_A] \sin\left(\frac{i\theta_{sk}}{2}\right), \text{ for } i = 3j-1 \\ 0, \text{ for } i = 3j \end{cases} \quad (10)$$

, respectively.

As shown in (8) and (10), for the $(i-1)^{\text{th}}$ on-load DC winding flux-linkage and hence induced voltage harmonic when $i=3j+1$, or $(i+1)^{\text{th}}$ on-load DC winding flux-linkage and hence induced voltage harmonic when $i=3j-1$, the ratio of its amplitude with skewing angle θ_{sk} to that without skewing, k_{ski} , can be given as,

$$k_{ski} = \frac{2}{i\theta_{sk}} \sin\left(\frac{i\theta_{sk}}{2}\right) \quad (11)$$

For the 6th on-load DC winding induced voltage harmonic caused by the 5th and 7th mutual inductances between the DC field winding and AC armature winding harmonics, they can be effectively suppressed by 80.90% and 86.36%, respectively, when $\theta_{sk}=60^\circ$, as shown in Fig. 3. It can be concluded from (11) that to effectively reduce the n^{th} on-load DC winding flux-linkage and hence induced voltage harmonic, meanwhile maintaining the open-circuit AC winding phase fundamental back-EMF and hence torque density, the optimal skewing angle θ_{sko} should be,

$$\theta_{sko} = \frac{2\pi}{N_{pe}} \quad (12)$$

As shown in TABLE II and (12), the optimal skewing angle θ_{sko} to reduce the on-load DC winding induced voltage should be 60° for all the analysed 12-stator-pole PS-WFSF machines having 10-, 11-, 13- and 14-rotor-pole rotors, as shown in TABLE IV.

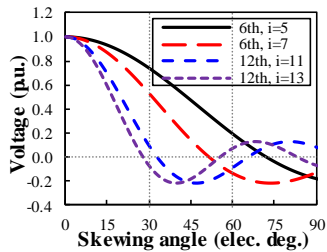


Fig. 3. Influence of skewing angle on on-load DC winding induced voltages harmonics.

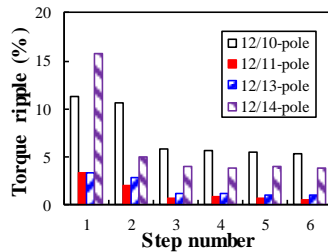


Fig. 4. Influence of step-skewing number on torque ripple ($\theta_{sk}=\theta_{sko}=60^\circ$).

TABLE IV
ANALYTICAL PREDICTION OF θ_{sko} FOR PS-WFSF MACHINES

Item	Unit	12-stator-pole PS-WFSF machines			
N_r	-	10	11	13	14
Open-circuit	°	60	30	30	60
Armature reaction	°	60	60	60	60
On-load	°	60	60	60	60

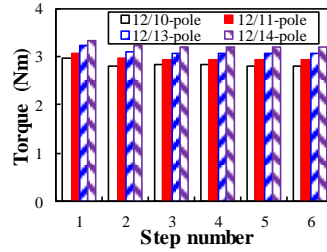


Fig. 5. Influence of step-skewing number N_{sk} on average electromagnetic torque ($\theta_{sk}=\theta_{sko}=60^\circ$).

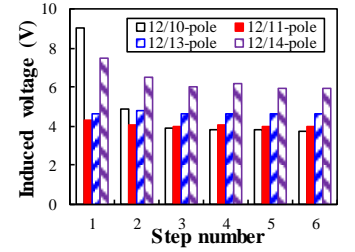


Fig. 6. Influence of step-skewing number on peak to peak value of the on-load DC winding induced voltages at 400r/min ($\theta_{sk}=\theta_{sko}=60^\circ$).

As shown in Fig. 4 and Fig. 5, skewing is indeed an effective way to reduce torque ripple but the average torque can be maintained. However, as shown in Fig. 6, when the step-skewing step number is $N_{sk}=6$ and $\theta_{sk}=\theta_{sko}=60^\circ$, on-load E_{pp} can be effectively reduced by 59.06% in the 12/10-pole PS-WFSF machine, but only 20.54% and 8.91% respectively in the 12/14- and 12/11-pole machines, even 1.04% higher in the 12/13-pole machine. This is due to the influence of current angle on M_{fA} , M_{fB} , and M_{fC} , which is neglected in (9) and (10). When the current angle is changed, the steel element permeability varies, resulting in a different M_{fA} , M_{fB} , and M_{fC} , as well as L_{ff} . As shown in Fig. 7, on-load E_{pp} varies with current angle in all the analyzed 4 machines. This is specifically explained for 12/13-pole PS-WFSF machine with $\theta_{sk}=\theta_{sko}=60^\circ$ and $N_{sk}=6$ as follows.

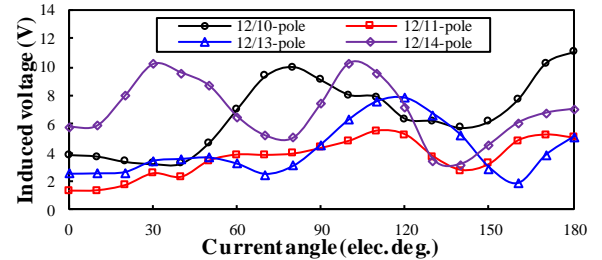


Fig. 7. Influence of current angle on peak to peak value of the on-load DC winding induced voltages at 400r/min.

As well known, compared with the open-circuit original ψ_{f1} without skewing, ψ_{f1} with a skew angle θ_s should lag θ_s . Based on this, the open-circuit E_{pp} can be effectively reduced to 0 by rotor continuously skewing [25]. This is also applicable for the on-load ψ_{f1} , if the influence of current angle on the steel element permeability is neglected. However, as shown in Fig. 8(a), ψ_{f1} with a skew angle θ_s not only lag the original one θ_s , but also distorted due to the impact of current angle on the on-load ψ_{f1} , resulting in that the total ψ_{f1} is even similar to the original one. This also similar to ψ_{f2} shown in Fig. 8(b). Consequently, as shown in Fig. 9, the total on-load E_{pp} with $\theta_{sk}=60^\circ$ is even 1.04% higher than the original one without

skewing.

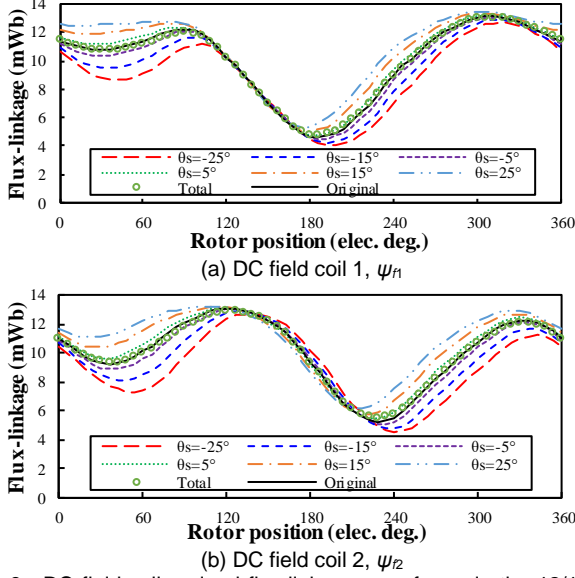


Fig. 8. DC field coil on-load flux-linkage waveforms in the 12/13-pole PS-WFSF machine with different θ_s for $\theta_{sk}=60^\circ$ and $N_{sk}=6$ at 400r/min.

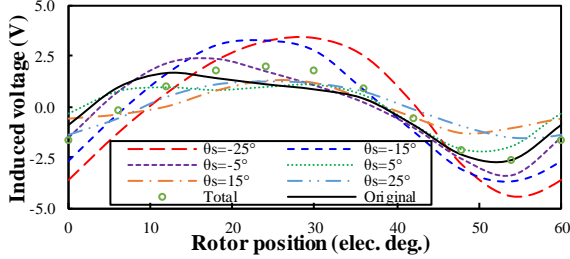


Fig. 9. On-load DC winding induced voltage in the 12/13-pole PS-WFSF machine with different θ_s for $\theta_{sk}=60^\circ$ and $N_{sk}=6$ at 400r/min.

TABLE V

CHARACTERISTICS OF 12-POLE PS-WFSF MACHINES WITHOUT AND WITH MODIFIED SKEWING

Item	Unit	12-stator-pole PS-WFSF machines			
N_r	-	10	11	13	14
Original on-load E_{pp}	V	9.06	4.32	4.58	7.46
Modified skew on-load E_{pp}	V	1.96	3.40	4.27	4.98
On-load E_{pp} reduction	%	78.42	21.25	6.96	33.34
Original T_{avg}	Nm	2.97	3.07	3.21	3.34
Modified skew T_{avg}	Nm	2.69	2.81	3.19	3.04
T_{avg} reduction	%	9.54	8.40	0.60	9.01
Original open-circuit E_{pp}	V	2.10	0.63	0.36	4.86
Modified skew open-circuit E_{pp}	V	0.36	0.10	0.08	1.15
Open-circuit E_{pp} reduction	%	82.72	84.10	77.86	76.23

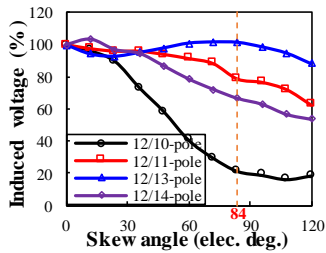


Fig. 10. Influence of skewing angle θ_{sk} on the on-load E_{pp} in 12-stator-pole PS-WFSF machines when $N_{sk}=6$ at 400r/min.

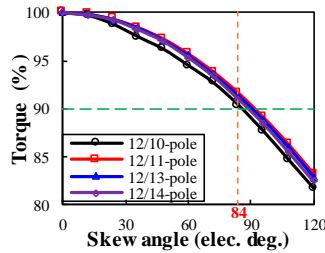


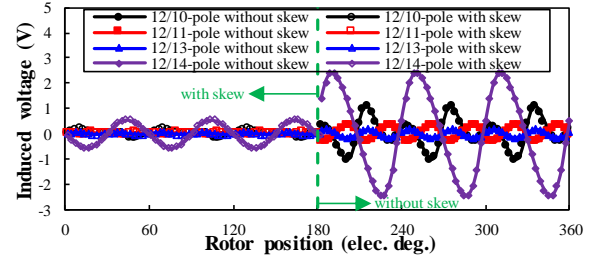
Fig. 11. Influence of skewing angle θ_{sk} on the T_{avg} in 12-stator-pole PS-WFSF machines when $N_{sk}=6$.

B. Modified Optimal Skewing Angle

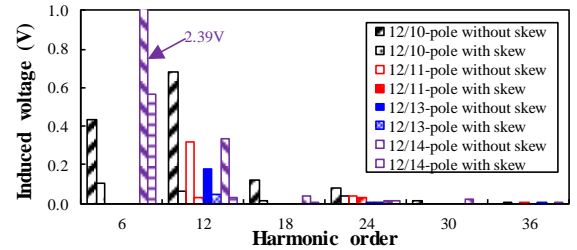
As shown in Fig. 10, by modifying the skew angle θ_{sk} , the on-load E_{pp} can be further reduced, compared with the $\theta_{sk}=60^\circ$. However, as shown in Fig. 11, the average torque T_{avg} will be smaller if θ_{sk} goes higher. To maintain more than 90% torque capability in the skewed machine, the highest reduction of the on-load E_{pp} can be reached as 78.42%, 21.25%, 6.96%, and 33.34% in the 12/10-, 12/11-, 12/13- and 12/14-pole PS-WFSF machines, when $\theta_{sk}=84^\circ$, 84° , 24° , and 84° , respectively, as shown in TABLE V.

As shown in TABLE V, by modifying the skewing angle θ_{sk} , the on-load E_{pp} in the 12/10-pole machine can be effectively reduced from 59.06% to 78.42%, whilst the average torque T_{avg} is 9.54% smaller than the original machine without skewing. However, after modifying the skewing angle θ_{sk} , the on-load E_{pp} in other 3 machines are still higher, which indicates that other methods need to be applied to reduce the on-load DC winding induced voltage.

As analysed in [25], the open-circuit E_{pp} can be theoretically reduced to zero by continuous rotor skewing with $\theta_{sk}=60^\circ$, 30° , 30° , and 60° for the 12/10-, 12/11-, 12/13- and 12/14-pole PS-WFSF machines, respectively. When the step skewing is applied, the open-circuit E_{pp} can be reduced by 98.59%, 95.20%, 94.13%, and 98.46% [25], respectively. When the skewing angle is for on-load condition, i.e. $\theta_{sk}=84^\circ$, 84° , 24° , and 84° for the 12/10-, 12/11-, 12/13- and 12/14-pole PS-WFSF machines, respectively, the open-circuit E_{pp} can be reduced 82.72%, 84.10%, 77.86% and 76.23%, respectively, as shown in Fig. 12 and TABLE V. This means the suppression of the open-circuit DC winding induced voltage will be slightly deteriorated, if the skewing angle is for on-load operation condition.



(a) Waveforms



(b) Spectra

Fig. 12. Open-circuit DC winding induced voltages of 12-stator-pole PS-WFSF machines without and with modified optimal skewing ($N_{sk}=6$).

IV. REDUCTION OF ON-LOAD DC WINDING INDUCED VOLTAGE BY ROTOR PAIRING

In this section, pairing of rotor iron piece to reduce the on-load DC winding induced voltage is investigated as follows.

As shown in Fig. 2(b), the main harmonics of the on-load DC winding induced voltages in the 12-stator-pole PS-WFSF machines are the 6th and 12th harmonics. As shown in Fig. 13(a), both the rotor iron piece outer arc θ_{ro} and the rotor iron piece inner arc θ_{ri} have an influence on the 6th and 12th harmonics amplitudes. However, when θ_{ro} varies, the initial phase of the 6th harmonics is always positive, as shown in Fig. 13(b). This means that the 6th harmonic cannot be smaller than both of those of the pairs by the rotor iron piece outer arc pairing, although the 12th harmonic can be reduced due to the bipolar initial phase waveform. However, when θ_{ri} varies, the initial phase waveforms of both the 6th and 12th harmonics are bipolar, as shown in Fig. 13(b). This indicates that the 6th and 12th harmonics of the on-load DC winding induced voltage can be reduced by rotor iron piece inner arc pairing. Indeed, since θ_{ro} mainly influence the outer air-gap permeance whilst θ_{ri} changes the inner one, θ_{ri} has a higher impact on the on-load DC winding induced voltage which is related to the inner air-gap permeance.

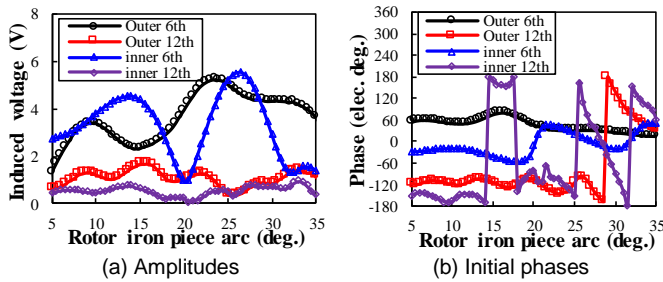


Fig. 13. Influence of rotor iron piece outer/inner arc on amplitudes and initial phases of the 6th and 12th on-load DC winding induced voltage harmonics in 12/10-pole PS-WFSF machine at 400r/min.

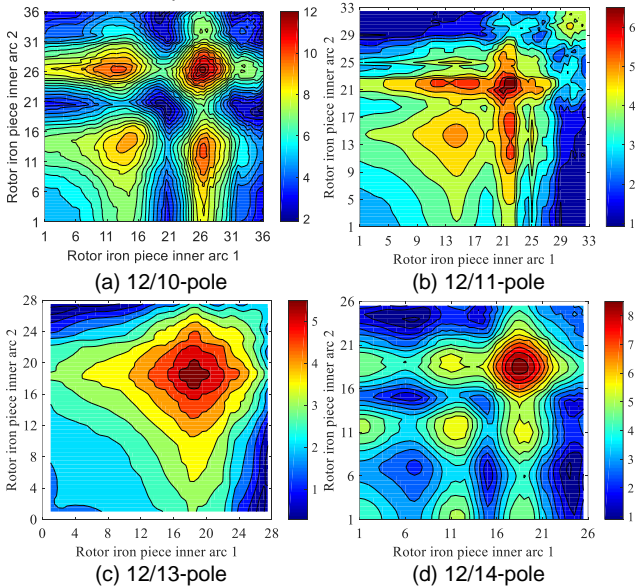


Fig. 14. Influence of paired rotor iron piece inner arcs on on-load E_{pp} .

As shown in Fig. 14, by designing two different rotor iron piece inner arcs axially, a smaller on-load E_{pp} can be achieved in all the analyzed 4 machines. However, the average electromagnetic torque will be smaller, as shown in Fig. 15. Here, it should be mentioned that the dimensional parameters of these 4 original machines are globally optimized for the largest average electromagnetic torque, as mentioned in [25]. The optimal combination of two rotor iron piece inner arcs θ_{ri1}

and θ_{ri2} is selected by two steps:

Step 1: If the average torque T_{avg} of a combination of θ_{ri1} and θ_{ri2} is smaller than 90% of the original T_{avg} , i.e. the highest T_{avg} , this combination is abandoned.

Step 2: Among the rest combinations of θ_{ri1} and θ_{ri2} of which the average torque is higher than 90% of the original T_{avg} , find out the optimal combination of θ_{ri1} and θ_{ri2} which has the highest on-load E_{pp} reduction.

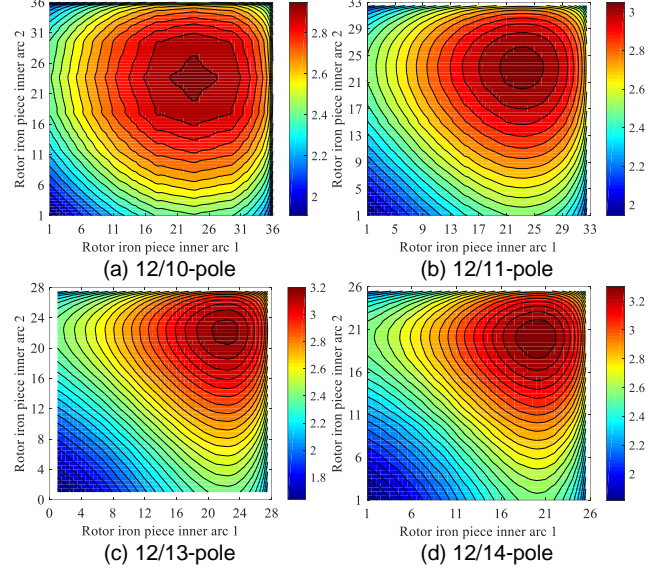


Fig. 15. Influence of paired rotor iron piece inner arcs on T_{avg} .

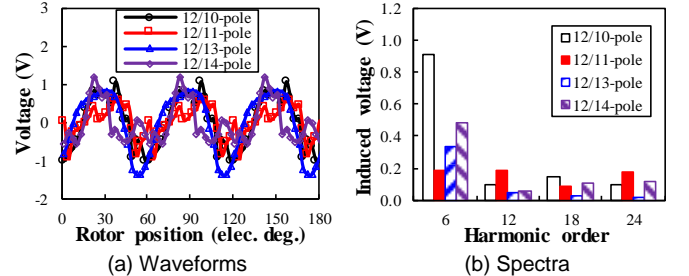


Fig. 16. On-load DC winding induced voltages after pairing at 400r/min.

TABLE VI

CHARACTERISTICS OF PS-WFSF MACHINES WITHOUT AND WITH PAIRING					
Item	Unit	12-stator-pole PS-WFSF machines			
N_p	-	10	11	13	14
Original on-load E_{pp}	V	9.06	4.32	4.58	7.46
Paired on-load E_{pp}	V	2.07	1.55	2.20	1.75
On-load E_{pp} reduction	%	77.16	64.11	52.12	76.49
Original T_{avg}	Nm	2.97	3.07	3.21	3.34
Paired T_{avg}	Nm	2.68	2.77	2.97	3.02
T_{avg} reduction	%	9.90	9.89	7.67	9.55

Based on these two steps, the optimal combinations of θ_{ri1} and θ_{ri2} are (19.5°, 35°), (15°, 31°), (21.5°, 27°), and (14.5°, 24°) for the 12/10-, 12/11-, 12/13- and 12/14-pole PS-WFSF machines, respectively. The on-load E_{pp} and T_{avg} of these 4 analyzed machines with optimal pairing are compared with the original counterparts without pairing in TABLE VI and Fig. 16. As shown in TABLE VI, by rotor iron piece inner arc pairing, the on-load E_{pp} in the 12/10-pole and 12/14-pole PS-WFSF machines can be effectively reduced by 77.16% and 76.49%, respectively. However, in the 12/11- and 12/13-pole machines, it can only be reduced by 64.11% and 52.12%, respectively. However, it should be noted that these results listed in TABLE

VI are based on keeping the 90% average torque. As shown in Fig. 14(b) and Fig. 14(c), in the 12/11- and 12/13-pole PS-WFSF machines the on-load E_{pp} can be reduced to further smaller, however the average torque T_{avg} after pairing will be smaller than 90% of the original T_{avg} .

V. COMPARISON OF DIFFERENT REDUCTION METHODS

The on-load E_{pp} and T_{avg} under two methods analyzed in the above sections are synthesized in TABLE VII and TABLE VIII, respectively. By using rotor skewing with $\theta_{sk}=60^\circ$, on-load E_{pp} in the 12/10-, 12/11- and 12/14-pole PS-WFSF machines can be reduced by 59.06%, 8.91% and 20.54%, respectively, whilst it is even 1.04% higher in the 12/13-pole counterpart as foregoing analysed.

TABLE VII

ON-LOAD E_{pp} IN 12-STATOR-POLE PS-WFSF MACHINES					
Item	Unit	12-stator-pole PS-WFSF machines			
N_r	-	10	11	13	14
Original on-load E_{pp}	V	9.06	4.32	4.58	7.46
Skewed on-load E_{pp} , $\theta_{sk}=60^\circ$	V	3.71	3.95	4.63	5.94
E_{pp} reduction, $\theta_{sk}=60^\circ$	%	59.06	8.91	-1.04	20.54
Modified skew on-load E_{pp}	V	1.96	3.40	4.27	4.98
E_{pp} reduction	%	78.42	21.30	6.98	33.36
Paired on-load E_{pp}	V	2.07	1.55	2.20	1.75
E_{pp} reduction	%	77.16	64.12	52.13	76.49

However, by modifying the skew angle θ_{sk} and maintaining 90% torque density of the original counterpart, on-load E_{pp} can be reduced by 78.42% for the 12/10-pole machine, whilst those for the 12/11-, 12/13- and 12/14-pole machines are still lower, i.e. 21.30%, 6.98% and 33.36%, respectively. By using rotor iron piece inner arc pairing, the on-load E_{pp} in the 12/10-, 12/11-, 12/13- and 12/14-pole machines can be reduced by 77.16%, 64.12%, 52.13%, and 76.49%, respectively, whilst the torque density can be maintained by as high as >90%. It is worth noting that in this paper the criteria to justify the effectiveness of the reduction method is a more than 50% reduction of on-load DC winding induced voltage and >90% torque being maintained.

TABLE VIII

ON-LOAD T_{avg} IN 12-STATOR-POLE PS-WFSF MACHINES					
Item	Unit	12-stator-pole PS-WFSF machines			
N_r	-	10	11	13	14
Original on-load T_{avg}	Nm	2.97	3.07	3.21	3.34
Skewed on-load T_{avg} , $\theta_{sk}=60^\circ$	Nm	2.81	2.94	3.07	3.18
T_{avg} reduction, $\theta_{sk}=60^\circ$	%	5.39	4.23	4.36	4.79
Modified skew on-load T_{avg}	Nm	2.69	2.81	3.19	3.04
T_{avg} reduction	%	9.43	8.47	0.62	8.98
Paired on-load T_{avg}	Nm	2.68	2.77	2.97	3.02
T_{avg} reduction	%	9.76	9.77	7.48	9.58

As deduced in Appendix B, the DC winding current ripple raised by the DC winding induced voltage will cause a fluctuated field excitation and hence additional harmonic components in the AC winding induced voltages, with average torque and torque ripple being impacted [26], despite of three-phase symmetric sinusoidal AC currents being implemented by current control. For example, according to (B. 2), the interaction between the 6th DC winding current harmonic and the 5th mutual inductance between the DC winding and the A-phase winding will cause additional components to the fundamental (6-5=1) and 11th (6+5=11)

harmonics of the A-phase winding induced voltage. Hence, both the average torque and the torque ripple will be changed due to the on-load DC winding induced voltage, considering the similar effect in B- and C-phase winding induced voltages. However, by modifying the skew angle θ_{sk} in the 12/10-pole PS-WFSF machine or using rotor iron piece inner arc pairing in all the four analysed PS-WFSF machines, most of the main on-load DC winding induced voltage harmonics can be effectively reduced, as shown in Fig. 17. In addition, according to (5), it can be concluded that the reduction of DC winding induced voltage harmonics shown in Fig. 17 is due to the suppression of the mutual inductance harmonics between the A-, B- and C-phase windings and the DC winding. Hence, the amplitudes of both the raised DC winding current harmonics I_{fi} and the mutual inductance harmonics M_i shown in (B. 2) will be suppressed by modifying the skew angle θ_{sk} in the 12/10-pole PS-WFSF machine or using rotor iron piece inner arc pairing in all the four analysed PS-WFSF machines, resulting less influence of on-load DC winding induced voltage on the AC winding induced voltages.

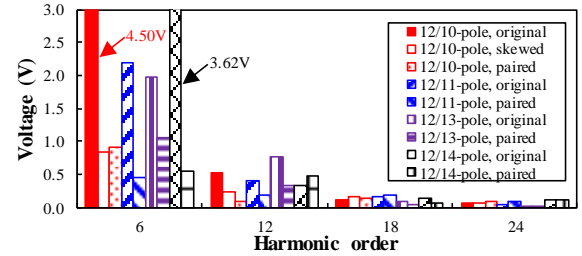


Fig. 17. Comparison of on-load DC winding induced voltage harmonics at 400r/min.

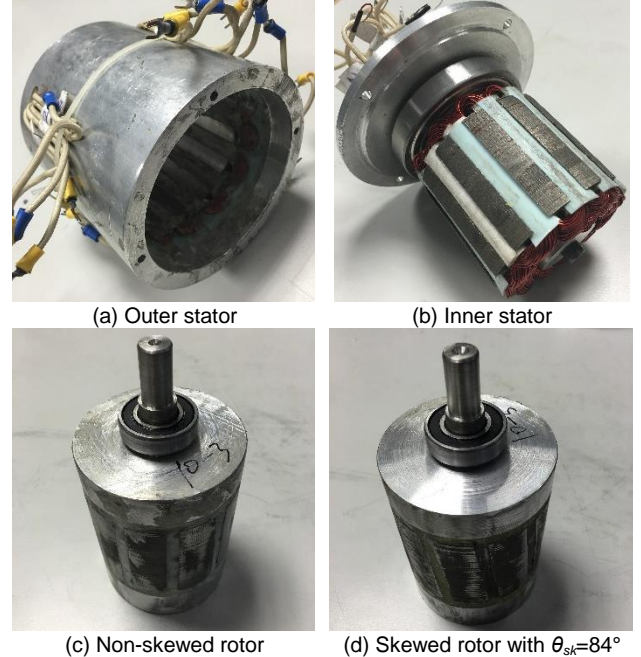


Fig. 18. Photos of the 12/10-pole PS-WFSF prototypes with non-skewed rotor and skewed rotor with $\theta_{sk}=84^\circ$.

VI. EXPERIMENTAL VALIDATION

To validate the foregoing analytical and FE analysis, the 12/10-stator/rotor-pole PS-WFSF machine with non-skewed rotor and skewed rotor with $\theta_{sk}=84^\circ$ are prototyped and tested

in this section. Fig. 18 shows the photos of different components of the prototypes with (a) outer stator, (b) inner stator, (c) non-skewed rotor and (d) skewed rotor with $\theta_{sk}=84^\circ$. It should be noted that a 0.5mm thick iron flux-bridge is introduced adjacent to the inner air-gap to connect the rotor iron pieces both rotors shown in Fig. 18(c)-Fig. 18(d).

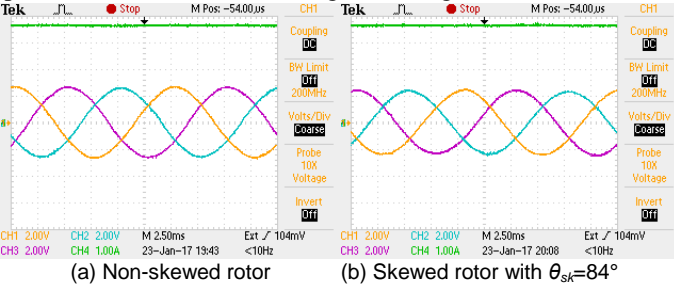


Fig. 19. Measured 3-phase open-circuit AC windings back-EMFs and DC winding current at 400r/min.

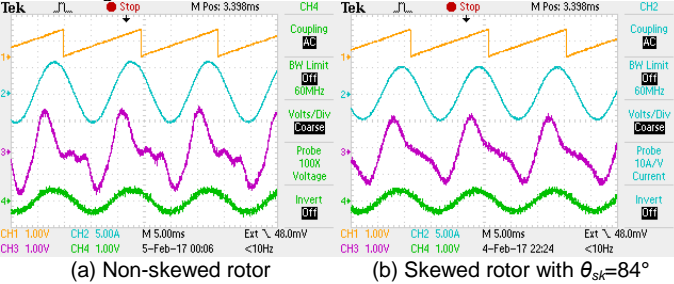


Fig. 20. Measured rotor electric position (CH1), phase A winding current (CH2), on-load DC coil 2 induced voltage (CH3) and phase A voltage (CH4) at 400r/min.

A. Constant Current Source for DC Winding

Since a constant DC winding current is the ideal aim of the closed-loop DC winding current control, both the previous analytical and FE analysis are based on a constant DC winding current. Hence, in this sub-section a constant current source for supplying the DC winding current is applied to validate the analytical and FE predicted results.

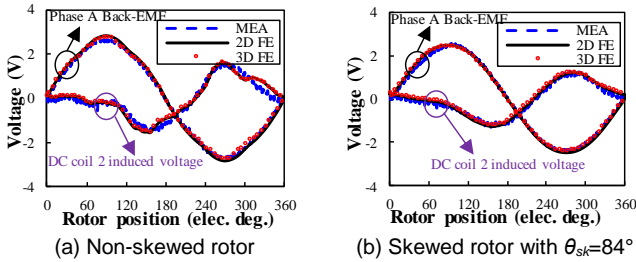


Fig. 21. Comparison of measured and FE predicted DC coil 2 induced voltage and phase A back-EMF waveforms at 400r/min.

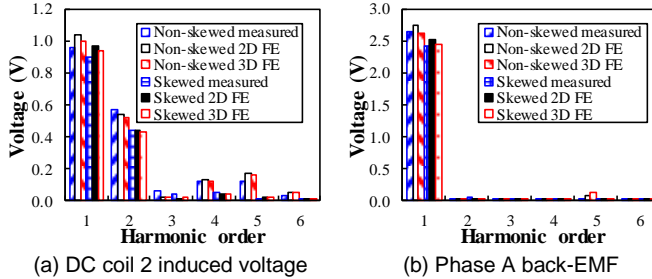


Fig. 22. Comparison of measured and FE predicted DC coil 2 induced voltage and phase A back-EMF harmonics at 400r/min.

The measured phase back-EMF waveforms of both prototypes at 400r/min are shown in Fig. 19. Similar to [25], to

avoid the influence of the DC current supply, not the on-load DC winding induced voltage but that of the DC coil 2 is measured to validate the analytical and FE analyses. When the PS-WFSF prototypes operate as generators with resistance load, the measured on-load DC coil 2 induced voltage waveforms at 400r/min are shown in Fig. 20, together with the rotor position, phase current and phase voltage. As shown in Fig. 21, both the measured on-load DC coil 2 induced voltage and the measured phase A back-EMF waveforms at 400r/min agree well with the 3D FE predicted results in both prototypes, although they are slightly smaller than the 2D FE values due to end effect. However, due to imperfect manufacturing, both the measured on-load DC coil 2 induced voltage and the measured phase A back-EMF harmonics at 400r/min are slightly different from the FE predicted harmonics, as shown in Fig. 22. As shown in Fig. 22(b), the measured phase A fundamental back-EMF in the prototype with skewing is 8.21% smaller than its counterpart without skewing, i.e. 2.41V and 2.63V, respectively.

Similar to the analysis in [25], based on the measured on-load DC coil 2 induced voltage waveforms shown in Fig. 20, those of the DC winding can be calculated as Fig. 23. As shown in Fig. 23, again due to imperfect manufacturing, in both prototypes the measured on-load DC winding induced voltage harmonics at 400r/min are distorted from their FE counterparts. However, the dominant measured on-load DC winding induced voltage 6th, 12th and 18th harmonics can be effectively reduced by 69.90%, 66.07% and 71.97%, respectively by rotor skewing.

As shown in Fig. 24, the measured static torques agree well with the 3D FE predicted results in both prototypes, although they are slightly lower than the 2D FE values due to end effect.

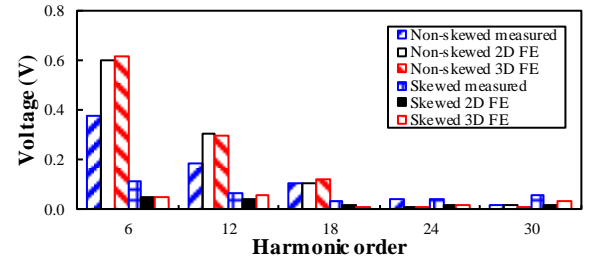


Fig. 23. Comparison of calculated on-load DC winding induced voltages harmonics based on the measured on-load DC coil 2 induced voltages at 400r/min.

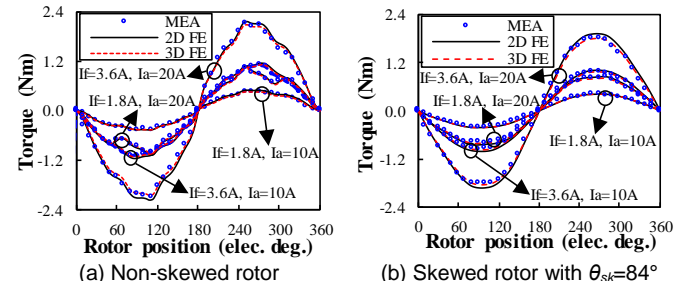


Fig. 24. Comparison of measured and FE predicted static torque waveforms ($I_s=-2I_b=-2I_c$).

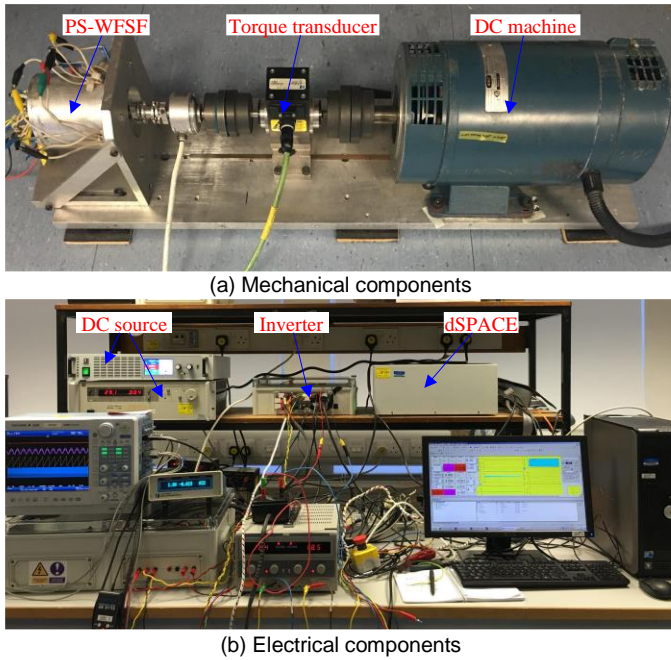


Fig. 25. Test platform of the PS-WFSF prototypes.

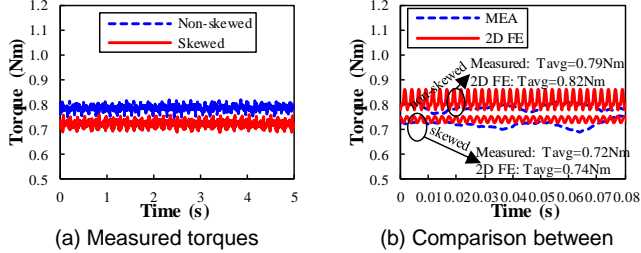


Fig. 26. Measured torques and the comparison with 2-D FE predicted values at 400r/min ($I_f=3.6A$, BLAC, $i_d=0$, $i_q=8A$).

B. H-Bridge for DC Winding

In this sub-section, the machine controller based test platform shown in Fig. 25 is used to measure the on-load shaft torque and the DC winding induced voltage, in which the DC winding voltage is supplied by a voltage source DC bus connected H-bridge with a closed-loop current control.

As shown in Fig. 26, compared with the prototype without skewing, the measured average shaft torque is reduced by 8.12% in the prototype with skewing, i.e. 0.79Nm and 0.72Nm, respectively. This is due to the reduction of AC windings phase fundamental back-EMF in Fig. 22(b) caused by rotor skewing. It is worth noting that the high shaft torque pulsations with fundamental mechanical frequency is due to the axial malalignment among mechanical components in Fig. 25(a).

As shown in Fig. 27, on-load DC winding current pulsation is larger than its open-circuit counterpart in both prototypes, since the armature reaction DC winding induced voltage is considerably larger than the open-circuit DC winding induced voltage. Although the measured on-load DC winding voltage waveforms of two prototypes shown in Fig. 27(c) and Fig. 27(d) contain PWM harmonics, the dominant measured on-load DC winding induced voltage 6th harmonic can be effectively reduced by utilizing rotor skewing, as shown in Fig. 28.

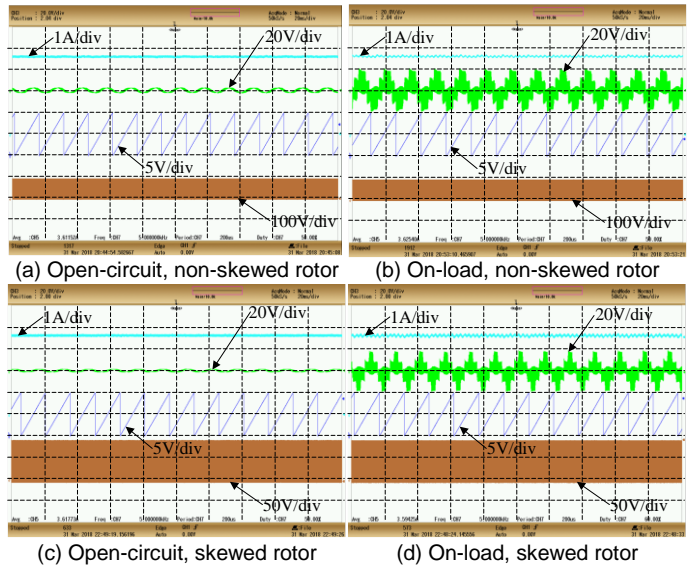


Fig. 27. Open-circuit and on-load DC winding current (top first, cyan), AC winding phase A back-EMF (top second, green), rotor position (top third, blue) and DC winding voltage (top fourth, bronze) at 400r/min when the DC winding is supplied by a H-bridge ($I_f=3.6A$).

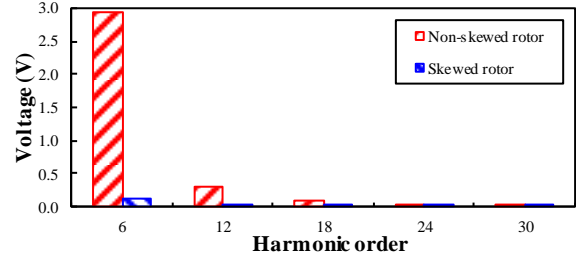


Fig. 28. Comparison of the on-load DC winding voltage harmonics at 400r/min when the DC winding is supplied by an H-bridge ($I_f=3.6A$).

VII. CONCLUSIONS

In this paper, on-load DC winding induced voltage in PS-WFSF machines is analyzed and two methods including skewing and pairing are proposed and comparatively analyzed to reduce the on-load DC winding induced voltages in the 12-stator-pole PS-WFSF machines having 10-, 11-, 13- and 14-rotor-pole rotors. The results show that the on-load DC winding induced voltage in the 12/10-pole PS-WFSF machine can be effectively reduced by modified rotor skewing or rotor pairing by 78.42% or 77.16%, respectively, whilst the torque density can both be maintained by more than 90%. As for the 12/11-, 12/13- and 12/14-pole PS-WFSF machines, the on-load DC winding induced voltage 64.12%, 52.13%, and 76.49%, respectively, whilst the torque density can also be maintained by >90%. Prototypes are built and tested to validate the analytical and FE results. Future works can be carried out to utilize these two methods together, i.e. skewing and pairing, to further reduce the on-load DC winding induced voltage, with better performance being possibly obtained.

APPENDIX A

Details of the three machines shown in TABLE I are given as follows.

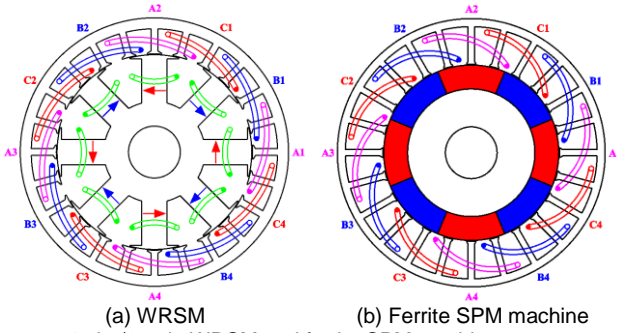


Fig. 29. 24-slot/8-pole WRSM and ferrite SPM machine.

TABLE IX

PARAMETERS OF 24-SLOT/8-POLE WRSM AND FERRITE SPM MACHINE

Item	Unit	WRSM	SPM machine
Stator yoke radius, R_{sy}	mm	40.75	42.58
Stator inner radius, R_{si}	mm	32.29	29.62
Stator tooth width, W_{st}	mm	4.02	2.23
Rotor pole width, W_{rp}	mm	8.77	N/A
Stator slot opening, O_{ss}	mm	1.70	1.83
Rotor slot opening, O_{rs}	mm	9.08	N/A
PM thickness, T_{PM}	mm	N/A	6.88
PM arc, θ_{PM}	°	N/A	45
PM remanence, B_r	T	N/A	0.41
PM coercive force, H_c	kAm	N/A	-250

TABLE X

PARAMETERS OF 12/10-POLE PS-WFSF MACHINE

Item	R_{osy}	R_{osi}	R_{ri}	R_{isy}	θ_{ost}	θ_{ot}	θ_{ro}	θ_{ri}	θ_{ist}	θ_{it}
Unit	mm	mm	mm	mm	°	°	°	°	°	°
Value	121.5	100.2	87.14	51.81	8.43	4.88	17.88	20.93	10.7	1.4

Since the AC winding pole-pair number of the 12/10-pole PS-WFSF machine is 4, the integer-slot 24-slot/8-pole conventional WRSM and the low-cost ferrite SPM machine having the slot number per pole per phase $q=1$ are taken for a comparison. All three machines have the same slot filling factor $k_{pf}=0.5$ and the same space envelop as the Toyota Prius 2010 IPM machine [24], i.e. stator outer radius $R_{so}=132\text{mm}$, stack length $l_s=50\text{mm}$, rotor inner radius $R_{ri}=25.5\text{mm}$, and air-gap width $g=0.87\text{mm}$. The main dimensional parameters of the WRSM and ferrite SPM machine shown in TABLE IX and those for the 12/10-pole PS-WFSF machine shown in TABLE X are optimized for the largest torque with a fixed winding current density $J_s=26.8\text{A/mm}^2$, the same as that of the Toyota Prius 2010 IPM machine [24]. The definitions of parameters shown in TABLE X can be referred in [25].

APPENDIX B

Influence of the on-load DC winding induced voltage on the AC armature windings is deduced as follows.

Considering the j^{th} DC winding current harmonic caused by the j^{th} on-load DC winding induced voltage, the DC winding current can be given by,

$$I_f(\theta_e) = I_{f0} + \sum_{j=6,12,18,\dots}^{\infty} I_{fj} \cos(j\theta_e + \theta_{fj}) \quad (\text{B.1})$$

where I_{f0} is the DC component. I_{fj} and θ_{fj} are the amplitude and initial phase of the j^{th} DC winding harmonic current, respectively.

Combining equations (5) and (B. 1), the A-phase winding flux-linkage due to DC winding current can be expressed as,

$$\begin{aligned} \psi_{Af}(\theta_e) &= I_f(\theta_e) M_{fA}(\theta_e) \\ &= I_{f0} \sum_{i=1,2,3,\dots}^{\infty} k_{wi} M_i \cos(i\theta_e + \theta_i) \\ &\quad + \frac{1}{2} \sum_{i=1,2,3,\dots}^{\infty} \sum_{j=6,12,18,\dots}^{\infty} k_{wi} M_i I_{fj} \{ \cos[(i \\ &\quad + j)\theta_e + \theta_i + \theta_{fj}] \\ &\quad + \cos[(i-j)\theta_e + \theta_i - \theta_{fj}] \} \end{aligned} \quad (\text{B.2})$$

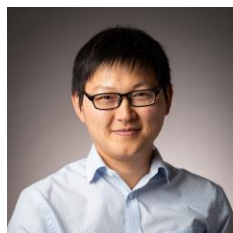
As shown in (B. 2), due to the interaction of the j^{th} DC winding current harmonic caused by the j^{th} on-load DC winding induced voltage and the i^{th} mutual inductance between the DC winding and the A-phase winding, i.e. M_{fA} shown in (5), additional components will be caused to the $i+j$ and $|i-j|$ harmonics of the A-phase winding induced voltage.

REFERENCES

- [1] I. Boldea, L. N. Tutelea, L. Parsa, and D. Dorrell, "Automotive electric propulsion systems with reduced or no permanent magnets: an overview," *IEEE Trans. Ind. Electron.*, vol. 61, no. 10, pp. 5696–5711, Oct. 2014.
- [2] G. Kronacher, "Design, performance and application of the vernier resolver," *The Bell Syst. Tech. Jour.*, vol. 36, no. 6, pp. 1487–1500, Nov. 1957.
- [3] C. H. Lee, "Vernier motor and its design," *IEEE Trans. Power Appa. and Syst.*, vol. 82, no. 66, pp. 343–349, Jun. 1963.
- [4] K. C. Mukherji and A. Tustin, "Vernier reluctance motor," *Proc. of IEE*, vol. 122, no. 4, pp. 965–974, Apr. 1975.
- [5] L. A. Agu and S. A. Nasar, "Universal reluctance machine with no rotor conductors," *IEE Jour. on Elec. Power Appl.*, vol. 2, no. 2, pp. 68–72, Apr. 1979.
- [6] S. Jia, R. Qu, J. Li, and D. Li, "Principles of stator DC winding excited vernier reluctance machines," *IEEE Trans. Energy Convers.*, vol. 31, no. 3, pp. 935–946, Sep. 2016.
- [7] S. Jia, R. Qu, J. Li, D. Li, and H. Lu, "Design considerations of stator dc-winding excited vernier reluctance machines based on the magnetic gear effect," *IEEE Trans. Ind. Appl.*, vol. 53, no. 2, pp. 1028–1037, Mar.-Apr. 2017.
- [8] T. Raminosoa, D. Torrey, A. M. El-Refaie, K. Grace, D. Pan, S. Grubic, K. Bodla, and K.-K. Huh, "Sinusoidal reluctance machine with DC winding: an attractive non-permanent magnet option," *IEEE Trans. Ind. Appl.*, vol. 52, no. 3, pp. 2129–2137, May-Jun. 2016.
- [9] A. Chiba, K. Kiyota, N. Hoshi, M. Takemoto, and S. Ogasawara, "Development of a rare-earth-free SR motor with high torque density for hybrid vehicles," *IEEE Trans. Energy Convers.*, vol. 30, no. 1, pp. 175–182, Mar. 2015.
- [10] Z. Q. Zhu and X. Liu, "Novel stator electrically field excited synchronous machines without rare-earth magnet," *IEEE Trans. Magn.*, vol. 51, no. 4, Apr. 2015, Art ID. 8103609.
- [11] C. Pollock, H. Pollock, R. Barron, J. R. Coles, D. Moule, A. Court, and R. Sutton, "Flux-switching motors for automotive applications," *IEEE Trans. Ind. Appl.*, vol. 42, no. 5, pp. 1177–1184, Sep./Oct. 2006.
- [12] C. Pollock, H. Pollock, R. Barron, J. R. Coles, D. Moule, A. Court, and R. Sutton, "Flux-switching motors for automotive applications," *IEEE Trans. Ind. Appl.*, vol. 42, no. 5, pp. 1177–1184, Sep./Oct. 2006.
- [13] J. T. Chen, Z. Q. Zhu, S. Iwasaki, and R. Deodhar, "Low cost flux-switching brushless AC machines," *Proc. Conf. Veh. Pow. Prop.*, France, 2010, pp. 1–6.
- [14] T. Fukami, Y. Matsuura, K. Shima, M. Momiyama, and M. Kawamura, "A multi-pole synchronous machine with nonoverlapping concentrated armature and field winding on the stator," *IEEE Trans. Ind. Electron.*, vol. 59, no. 6, pp. 2583–2591, Jun. 2012.
- [15] Y. Tang, J. J. H. Paulides, T. E. Motosca, and E. A. Lomonova, "Flux switching machine with DC excitation," *IEEE Trans. Magn.*, vol. 48, no. 11, pp. 3583–3586, Nov. 2012.
- [16] Z. Q. Zhu, Y. J. Zhou, J. T. Chen, and J. E. Green, "Investigation of nonoverlapping stator wound-field synchronous machines," *IEEE Trans. Energy Convers.*, vol. 30, no. 4, pp. 1420–1427, Dec. 2015.
- [17] K. Boughrara, T. Lubin, and R. Ibtouen, "General subdomain model for predicting magnetic field in internal and external rotor multiphase

flux-switching machines topologies,” *IEEE Trans. Magn.*, vol. 49, no. 10, pp. 5310–5325, Oct. 2013.

- [18] B. Gaussens, E. Hoang, O. de la Barrière, J. Saint-Michel, M. Lecrivain, and M. Gabsi, “Analytical approach for air-gap modeling of field-excited flux-switching machine: no-load operation,” *IEEE Trans. on Magn.*, vol. 48, no. 9, pp. 2505–2517, Sep. 2012.
- [19] B. Gaussens, E. Hoang, O. de la Barrière, J. Saint-Michel, P. Manfe, M. Lecrivain, and M. Gabsi, “Analytical armature reaction field prediction in field-excited flux-switching machines using an exact relative permeance function,” *IEEE Trans. on Magn.*, vol. 49, no. 1, pp. 628–641, Jan. 2013.
- [20] E. Sulaiman, T. Kosaka, and N. Matsui, “A new structure of 12 slot-10 pole field-excitation flux switching synchronous machine for hybrid electric vehicles,” in *Proc. 14th Eur. Conf. Power Electron. Appl.*, Birmingham, UK, Aug.-Sep. 2011, pp. 1–10, paper 245.
- [21] E. Sulaiman, T. Kosaka, and N. Matsui, “Design study and experimental analysis of wound field flux switching motor for HEV applications,” in *Proc. IEEE Inter. Conf. Elec. Mach.*, France, Sep. 2012, pp. 1269–1275.
- [22] T. Raminosoa, A. M. El-Refaie, D. Pan, K. K. Huh, J. P. Alexander, K. Grace, S. Grubic, S. Galioto, P. B. Reddy, and X. Shen, “Reduced rare-earth flux-switching machines for traction applications,” *IEEE Trans. Ind. Appl.*, vol. 51, no. 4, pp. 2959–2971, Jul.-Aug. 2015.
- [23] Z. Q. Zhu, Z. Z. Wu, D. J. Evans, and W. Q. Chu, “A wound field switched flux machine with field and armature windings separately wound in double stators,” *IEEE Trans. Energy Convers.*, vol. 30, no. 2, pp. 772–783, Jun. 2015.
- [24] T. A. Burrell *et al.*, “Evaluation of the 2010 Toyota Prius hybrid synergy drive system,” Oak Ridge Nat. Lab., Oak Ridge, TN, USA, Rep. ORNL/TM2010/253, 2011.
- [25] Z. Z. Wu, Z. Q. Zhu, C. Wang, J. C. Mipo, S. Personnaz, and P. Farah, “Reduction of open-circuit DC winding induced voltage in wound field switched flux machines by skewing,” *IEEE Trans. Ind. Electron.*, pp. 1715–1726, vol. 66, no. 3, Mar. 2019.
- [26] A. Zulu, B. Mecrow, and M. Armstrong, “A wound-field three-phase flux-switching synchronous motor with all excitation sources on the stator,” *IEEE Trans. Ind. Appl.*, vol. 46, no. 6, pp. 2363–2371, Nov./Dec. 2010.
- [27] C. Yu and S. Niu, “Development of a magnetless flux switching machine for rooftop wind power generation,” *IEEE Trans. Energy Convers.*, vol. 30, no. 4, pp. 1703–1711, Dec. 2015.
- [28] W. Fei and P. C. K. Luk, “A new technique of cogging torque suppression in direct-drive permanent-magnet brushless machines,” *IEEE Trans. Ind. Appl.*, vol. 46, no. 4, pp. 1332–1340, Jul.-Aug. 2010.
- [29] I. Petrov, P. Ponomarev, Y. Alexandrova, and J. Pyrhönen, “Unequal teeth widths for torque ripple reduction in permanent magnet synchronous machines with fractional-slot non-overlapping windings,” *IEEE Trans. on Magn.*, vol. 51, no. 2, pp. 1–9, Feb. 2015, Art. ID 8100309.
- [30] T. H. Kim, S. H. Won, K. Bong, and J. Lee, “Reduction of cogging torque in flux-reversal machine by rotor teeth pairing,” *IEEE Trans. on Magn.*, vol. 41, no. 10, pp. 3964–3966, Oct. 2005.



Z. Z. Wu (S'15-M'18) received the B.Eng. and M.Sc. degrees in electrical engineering from Southeast University, Nanjing, China, in 2010 and 2013, respectively, and the Ph.D. degree in electrical and electronic engineering from The University of Sheffield, Sheffield, U.K., in January 2017.

Since August 2018, he has been with Powertrain and Vehicle Research Centre, Department of Mechanical Engineering,

University of Bath, Bath, U.K., where he is currently a Prize Fellow in Electric Propulsion. His major research interests include the advanced electrical machines and drives for electric propulsion systems.

From January 2017 to August 2018, he was with Warwick Manufacturing Group (WMG), University of Warwick, Coventry, U.K., as a research fellow in electrical machines.



Z. Q. Zhu (M'90–SM'00–F'09) received the B.Eng. and M.Sc. degrees in electrical and electronic engineering from Zhejiang University, Hangzhou, China, in 1982 and 1984, respectively, and the Ph.D. degree in electrical and electronic engineering from The University of Sheffield, Sheffield, U.K., in 1991.

Since 1988, he has been with The University of Sheffield, where he is currently a Research Chair of the Royal Academy of Engineering/Siemens with the Department of

Electronic and Electrical Engineering and the Head of the Electrical Machines and Drives Research Group. His current research interests include the design and control of permanent-magnet brushless machines and drives for applications ranging from automotive through domestic appliances to renewable energy.

Dr. Zhu is a Fellow of the Royal Academy of Engineering.



C. Wang received the B.Eng. and M.Sc. degrees in electrical engineering from Hefei University of Technology, Hefei, China, in 2008 and 2011, respectively. He is currently working toward the Ph.D. degree in electronic and electrical engineering from the University of Sheffield, Sheffield, U.K.

From 2011 to 2015, he was an Engineer at Midea Welling Motor Technology Company, Ltd., Shanghai, China. His research interests include the control of electric drives.



J. C. Mipo received the Ph.D. degree in electrical engineering from Pierre-and-Marie-Curie University, Paris, France.

Since 1998, he has been with Valeo Engine and Electrical Systems, Creteil, France, where he is currently an Advanced Technical Manager.



S. Personnaz received the Ph.D. degree in electric engineering from the Laboratoire d'Electrotechnique de Grenoble, Grenoble, France, in 1992.

Since 2017, she has been with Valeo Engine and Electrical Systems, Creteil, France, where she is currently the PES Electrotechnical Director, one of Powertrain Electrical System core activity. She leads the team of electric machine designers for the

low voltage applications.



P. Farah received the Ph.D. degree in electrical engineering from the Institute National Polytechnique de Grenoble, France, in 1995.

From 2013 to 2016, he was with Valeo Engine and Electrical Systems, Creteil, France, as the Director of the Electromagnetic Design Group.